RESEARCH ARTICLE

NANO · MICRO small
www.small-journal.com

Emergence of Robust 1D Atomic and Electronic Textures in Mn Ultrathin Films via Antiferromagnet-Ferromagnet Interfaces

Eiichi Inami, Peter Krüger, Hiroki Hayashi, and Toyo Kazu Yamada**

1D electronic structures on 2D crystalline surfaces are crucial for investigating low-dimensional quantum phenomena and enabling the development of dimensionally engineered nanodevices. However, the inherent periodic symmetry of 2D atomic lattices generally leads to delocalized electronic band extending across the surface, making the creation of periodic 1D electronic states a significant challenge. Here, robust 1D electronic ordering is demonstrated in ultrathin Mn films grown on an atomically flat, non-reconstructed body-centered cubic Fe substrate. Scanning tunneling microscopy and spectroscopy revealed stripe-like patterns aligned along the [1$\bar{1}$0] direction, with periodicities of 2.5 and 5 atomic rows in the Mn monolayer and bilayer, respectively. The bilayer further exhibits energy-dependent phase variations. Density functional theory indicates that magnetic frustration in the quasi-hexagonal Mn lattice drives out-of-plane atomic displacements, stabilizing the 1D order. The resulting electronic textures are stable at room temperature and resilient to defects. These findings establish a platform for designing intrinsic 1D electronic patterns in 2D films, with broad implications for spintronics, quantum devices, and molecular-scale engineering.

1. Introduction

Controlling the dimensionality of electronic states on 2D surfaces has remained a significant challenge over decades. This capability is key to advance next-generation quantum and nanoscale technologies, including quantum computing, spintronics, molecular and superconducting electronics, which often rely on low-dimensional platforms such as quantum dots, quantum wires, and van der Waals materials.[1–9] In particular, achieving 1D electronic ordering on 2D surface could enable anisotropic quantum transport and support quantum-confined functional units for nanoscale device integration.[6,7] However, the periodic symmetry of crystalline 2D surfaces typically leads to delocalized electronic bands extending across the surface, making it difficult to stabilize intrinsic 1D electronic states. Although noble metal surfaces can undergo surface reconstructions that introduce atomic corrugations on the order of 10–20 pm,[10] such subtle distortions generally fail to produce significant electronic anisotropy, and the resulting surface states retain essentially 2D nature.

To overcome this limitation, various symmetry-breaking strategies have been explored, including the introduction of atomic-scale defects such as vicinal steps, missing rows, and adsorbed atoms and molecules. In the case of atomic steps, 2D surface states can be quenched,[11,12] and 1D-like features appear when atoms or molecules align along step edges.[13–18] However, these features typically arise from the adsorbate chains themselves and do not reflect intrinsic 1D states of the surface. Another strategy is confining surface electrons within nanoscale boundaries, so-called quantum corrals,[19,20] using single atoms, 2D metal–organic frameworks[21–24] and covalent organic cages.[25–27] Yet, despite these efforts, no clear demonstration of 1D electronic ordering has been achieved through such approaches.

More recently, 1D electronic order has been realized on the 2D surfaces of layered van der Waals materials such as transition metal dichalcogenides. For example, 2H-$NbSe_2$, which typically exhibits a 3 × 3 2D charge density wave (3Q-CDW), can transition into a 1D striped CDW phase (1Q-CDW)[28–30] under large strain and weak magnetic fields.[31–33] However, this transition relies on a finely tuned combination of symmetry breaking, a quasi-hexagonal array of Nb atoms, and strong spin-orbit coupling from the surrounding chalcogenide layers. This highlights the delicate conditions required to stabilize 1D electronic phases, even in intrinsically low-dimensional, correlated materials.

E. Inami, P. Krüger, H. Hayashi, T. K. Yamada
Department of Materials Science
Chiba University
1-33 Yayoi-cho, Inage-ku, Chiba 263-8522, Japan
E-mail: inami.eiichi@kochi-tech.ac.jp; toyoyamada@faculty.chiba-u.jp
E. Inami
School of Systems Engineering
Kochi University of Technology
185 Miyanokuchi, Tosayamada, Kami, Kochi 782-8502, Japan
P. Krüger, T. K. Yamada
Molecular Chirality Research Centre
Chiba University
1-33 Yayoi-cho, Inage-ku, Chiba 263-8522, Japan

The ORCID identification number(s) for the author(s) of this article can be found under https://doi.org/10.1002/smll.202504791

DOI: 10.1002/smll.202504791

In this study, we demonstrate that even conventional 3*d* transition metals, ferromagnetic (FM) Fe and antiferromagnetic (AFM) Mn, can give rise to 1D atomic stripe patterns in the local density of states (LDOS) on a 2D surface. Realizing this phase requires precise control over Mn film growth on Fe surfaces. For comparison, Mn films grown on Fe(001)[34–40] form atomically flat body-centered tetragonal (bct) structures with uniformly aligned in-plane spins. This uniform spin configuration arises because the relatively large Mn—Mn spacing weakens intralayer magnetic coupling, allowing the Mn—Fe interfacial interaction to dominate. Given these insights, we employed a body-centered cubic (bcc)-Fe(110) whisker substrate, which facilitates the growth of more densely packed Mn films with shorter Mn—Mn spacing than in the Mn/Fe(001) system. This structural configuration leads to competition between interfacial Mn-Fe and intralayer Mn—Mn spin interactions, giving rise to magnetic frustration that enables the emergence of robust 1D electronic stripe patterns on the 2D Mn(110) surface.

2. Results

2.1. Stripe Patterns in Ultrathin Mn Films on Fe(110)

Mn films were grown on a Fe(110) surface at 300 K in an ultrahigh vacuum (UHV) preparation chamber. The prepared sample was subsequently transferred into the analytical chamber without breaking the UHV condition. Scanning tunneling microscopy (STM) and scanning tunneling spectroscopy (STS) measurements were performed at 78 and 300 K (**Figure 1a**). The detailed experimental methods are provided in the"Experimental" Section.

Figure 1b–d present large-scale STM topographies (170×170 nm^2) of the Fe(110) surface observed at 78 K, where Figure 1b shows the pristine Fe(110) surface, whereas Figure 1c,d show the surface following the deposition of 0.5 and 1.2 monolayers (MLs) of Mn, respectively. Before Mn deposition (Figure 1b), the Fe(110) surface exhibited atomically flat terraces exceeding 100 nm in size. An atomically-resolved STM image highlights a centrally positioned rectangular bcc (110) lattice unit (inset of Figure 1b). In Figure 1e, the height profile along line A in Figure 1b reveals a step with a height of ≈0.2 nm. This is consistent with the spacing between Fe(110) layers, calculated based on the lattice constant of bcc-Fe ($a = 0.2866$ nm),[12] thus confirming the presence of single atomic steps.

The Mn atoms deposited onto these Fe(110) terraces formed atomically flat monolayer (Mn_{1st}) islands, as shown in Figure 1c. Intriguingly, these islands were predominantly formed on the terrace areas, with negligible contact with the steps. This suggests that Mn islands grow through the aggregation of diffusing Mn atoms on terrace areas. Figure 1c also reveals the elongated shape of these islands, indicating that Mn islands tend to grow preferentially in the [1$\bar{1}$0] direction rather than the [001] direction. In Figure 1e, the height profile along line B in Figure 1c reveals an apparent height of the island to be ≈0.26 nm, ≈30% (0.06 nm) higher than the Fe(110) single-step height. This also indicates that the islands are composed of adsorbed Mn atoms, as depicted with light-blue shading in Figure 1e.

At the 1.2 MLs coverage (Figure 1d), the Fe(110) substrate was almost entirely covered by the Mn_{1st} layer, above which the second Mn islands (referred to as Mn_{2nd} island) started to emerge, exhibiting shapes similar to those of Mn_{1st} islands. The height profile along line C in Figure 1d reveals that the apparent height of the Mn_{2nd} island (≈0.24 nm) was ≈8% lower than that of the Mn_{1st} but 20% larger than the Fe(110) interlayer distance (0.2 nm). As discussed later, the variation in layer heights between Mn_{1st} and Mn_{2nd} islands is attributed to a combination of differences in electronic structures and interatomic interactions between Mn_{1st}-Fe and Mn_{2nd}–Mn_{1st}. The former contributes to an apparent height difference, while the latter results in an actual topographical difference.

The magnified STM images in Figure 1f,g elucidated key features of the Mn/Fe(110) systems. These images reveal distinctive 1D stripe patterns along the [1$\bar{1}$0] direction both on the Mn_{1st} and Mn_{2nd} islands. These stripe patterns remain stable at room temperature (see Figure S1, Supporting Information), indicating their thermal robustness. The results suggest that structural and electronic modulations within the Mn island arise from the competing interactions: frustration between Mn-Mn interactions within the islands and/or Mn—Fe interactions at the substrate interface.

Figure 1f,g also reveals the presence of defects within the Mn_{1st} and Mn_{2nd} islands. Their types were further characterized in STM images in Figure S2a (Supporting Information) which shows a distinct stripe pattern with small and large dark spots. Each defect exhibits a different LDOS, suggesting local symmetry and chemical composition variation. In the observed area, ≈40 small dark spots were identified among an estimated 700 Mn atoms, corresponding to a defect ratio of ≈6% (40/700). These small dark spots align with the Fe(110) crystalline direction [1$\bar{1}$0], indicating that they likely originate from intermixed Fe atoms embedded within the Mn layer. In contrast, the large dark spots, far rarer (< 1%), are likely attributable to impurity atoms.

2.2. Electronic Structures of Ultrathin Mn Films on Fe(110)

We focus our analysis on the Mn_{1st} layer to investigate the electronic properties associated with the observed stripe pattern. Figure 2a–d presents the STM topography of Mn_{1st} island on Fe(110) terrace (**Figure 2a**) and the simultaneously acquired differential conductance (dI/dV) maps (Figure 2b-d) at sample biases of −250, −50, and +250 mV (setpoint bias of $V_s = -1$ V), respectively. Complete dI/dV maps are available in Video S1 (Supporting Information). Notably, the stripes patterns evident in the dI/dV map are exclusive to the Mn_{1st} island and absent on the Fe(110) surface. It was also confirmed that the stripe patterns remained constant across different bias voltages, as further elucidated by Figure 2e, highlighting the stripe pattern within the boxed area B in Figure 2b at representative bias voltages.

To fully understand the bias-dependent characteristics, we analyzed the dI/dV intensity profile along the [001] direction (line A-A' in Figure 2e) across all biases within the dI/dV dataset. Figure 2f presents the resultant 3D dI/dV profile map as a function of energy (*y*-axis) and position (*x*-axis), where the profile at each bias was normalized to the range of [0, 1] to amplify the visibility of the stripe structure (results without normalization are provided in Figure S3a, Supporting Information). This 3D view highlights that, within the bias range of −0.4–+0.7 V, the

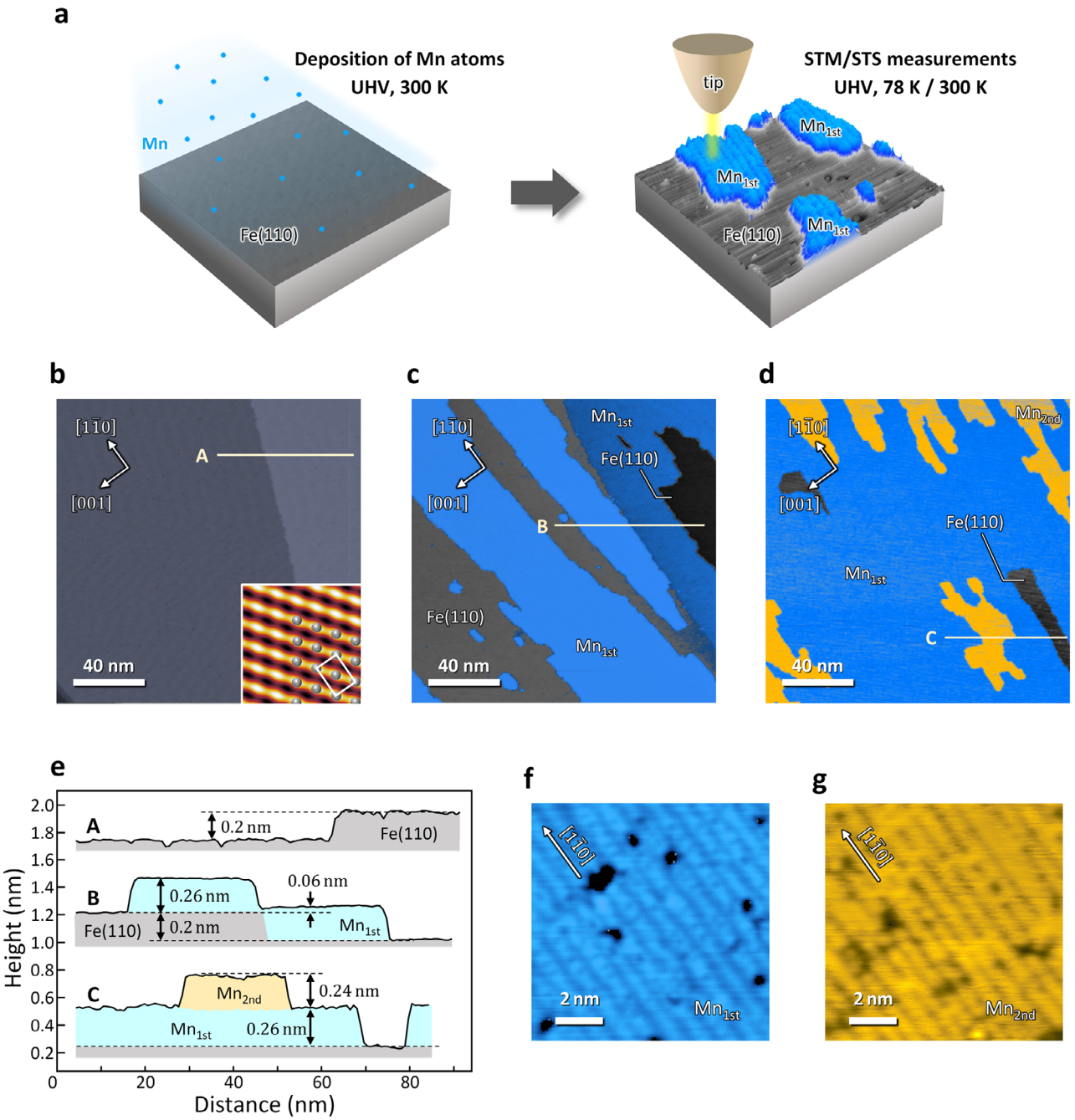

Figure 1. STM results of Mn monolayers and bilayers on bcc Fe(110). a) Sketches showing Mn atom deposition on Fe(110) surface (left) and the subsequent STM/STS analysis, revealing surface morphology and local electronic structures. b-d) STM topographies of pristine Fe(110) surface, Fe(110) surface with 0.5 MLs coverage of Mn atoms, Fe(110) surface with 1.2 MLs coverage of Mn atoms. The STM images were acquired over 170 × 170 nm^2 areas with a sample bias of −1.0 V and tunneling current of 100 pA. The inset in **b** shows a high-pass filtered STM image resolving the atomic arrangement of the Fe(110) surface, with an atomic model of the Fe(110) surface superimposed. e) Height profiles along the lines A, B, and C indicated in **b–d**. f,g) High-resolution STM topographies acquired on the Mn monolayer, and on the Mn bilayer.

stripe periodicity along the [001] direction remains constant at $\lambda = 0.72 \pm 0.15$ nm. This value corresponds to ≈2.5 times the interatomic distance of substrate Fe atoms along the [001] direction (0.286 nm).

To elucidate the electronic origin of the stripe pattern, normalized dI/dV spectra, indicative of the LDOS,[41,42] were analyzed, as shown in Figure 2g. These spectra were examined at the ridge (marked 'R' in Figure 2f), the trench (labeled 'T' in Figure 2f) of the Mn_{1st} island, and the Fe(110) terrace (boxed area A in Figure 2b). Following Gaussian fitting, distinctive peaks near the Fermi energy were identified in both the R and T areas of the Mn_{1st} island, located at ≈0.15 and 0.19 eV, respectively. These

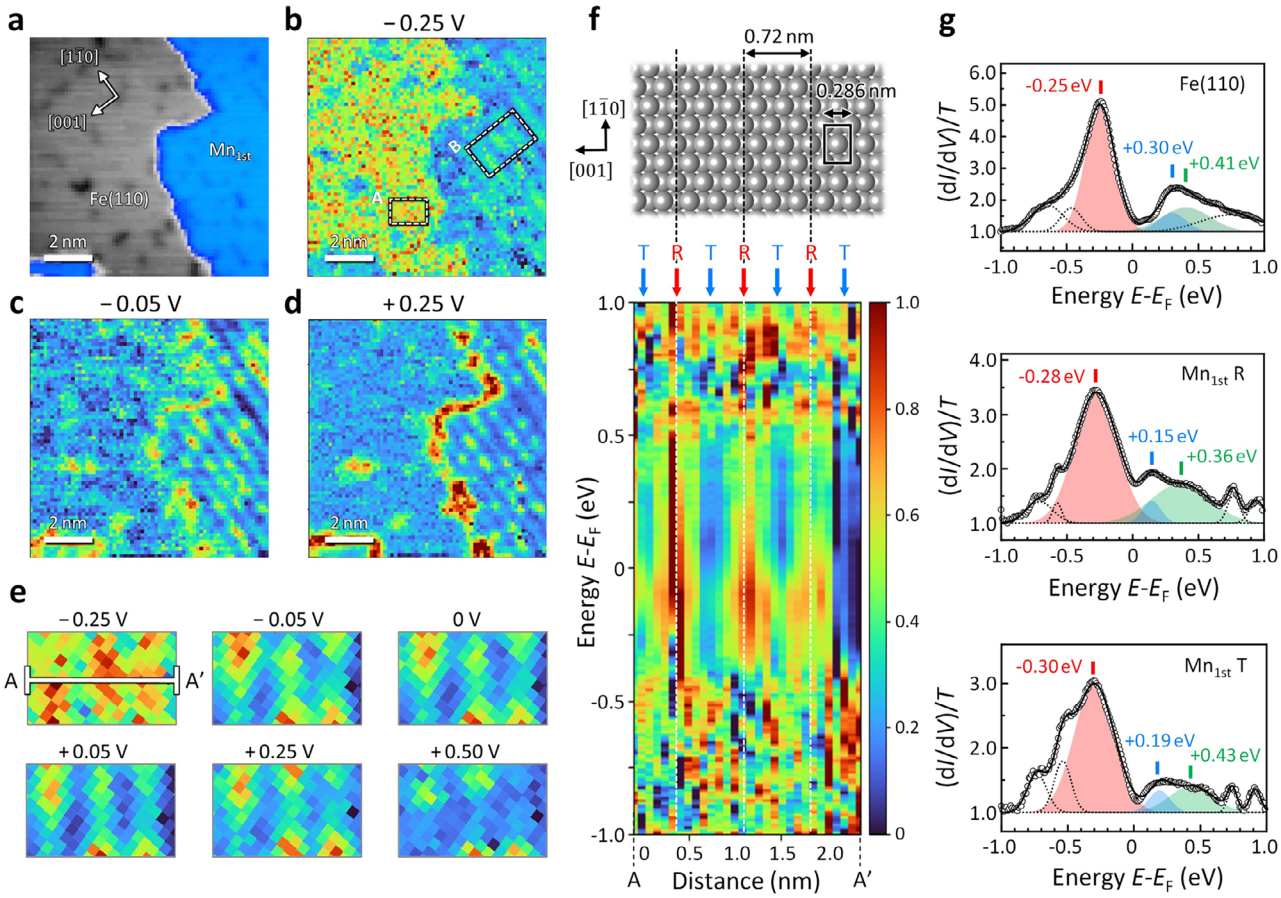

Figure 2. Electronic structure of Mn monolayer on bcc Fe(110). a) STM topography of a Mn monolayer on Fe(110) surface, imaged at a sample bias of −1.0 V. b–d) dI/dV maps obtained simultaneously with **a**, at sample biases of −250, −50 mV, +250 mV. Images **a-d** cover the same 9.9 × 9.9 nm^2 area. e) dI/dV maps at various characteristic bias voltages, extracted from a boxed area B in **b**. f) dI/dV profile map along line A-A' in **e**, as a function of energy relative to the Fermi level (E_F). Each profile is normalized within [0, 1]. At the top of **d**, the atomic structural model of the Fe(110) surface is shown for reference. Arrows labeled 'T' and 'R' highlight the trench and ridge areas in the stripe pattern, respectively. g) Normalized dI/dV spectra at the Fe(110) surface (boxed area A in **b**), R, and T areas. The spectral peak positions near Fermi Energy, marked by red, blue, and green ticks, were derived from Gaussian fitting analysis.

peaks, absent in the Fe(110) area, indicate intrinsic features to the Mn_{1st} island (a direct comparison of the dI/dV spectra is provided in Figure S4b, Supporting Information). Notably, the two peaks at the R and T area are not identical, exhibiting a slight offset of ≈40 meV. This offset cannot be attributed to thermal fluctuations as the thermal energy of k_BT is ≈7 meV at 78 K. Instead, it indicates an inherent difference in electronic structure, suggesting subtle variations in the atomic arrangement between the R and T areas.

An interesting stripe pattern was further observed on the Mn_{2nd} island. **Figure** 3a–d show STM topography, including Mn_{1st} and Mn_{2nd} islands (Figure 3a), and the simultaneously obtained dI/dV spectroscopy maps at sample biases of −250, −50, and +250 mV (setpoint bias of V_s = −1 V), respectively. Complete dI/dV maps are available in Video S2 (Supporting Information). The three dI/dV maps (Figure 3b–d) confirm the presence of periodic stripes parallel to the [1$\bar{1}$0] orientation on both the Mn_{1st} and Mn_{2nd} islands. However, it is essential to note that the appearance of the stripe pattern on the Mn_{2nd} island shows significant changes depending on the sample bias. This is also confirmed clearly in Figure 3e, where the stripe pattern in the boxed area in Figure 3b is highlighted at the representative sample bias voltage. Analogous to Figure 2f, we analyzed the normalized dI/dV intensity profile map along the [001] direction (line B-B' in Figure 3e), with the result shown in Figure 3f (unnormalized result is available in Figure S3b, Supporting Information). In contrast to the Mn_{1st} island, the stripe periodicity on the Mn_{2nd} island changed significantly, six times within the bias range of −1–1 V, exhibiting a diverse stripe pattern. Careful inspection of Figure 3f also revealed that, depending on the voltage, the stripe's periodicities can be either 0.72 ± 0.07 nm (λ) or double, 1.44 ± 0.22 nm (2λ). These results definitively indicate that the lattice translation symmetry of the Mn_{2nd} island along the [001] direction is 1.44 nm, which is twice that of the Mn_{1st} layer (0.72 nm) and five times that of the Fe(110) substrate.

The bias-dependent stripe pattern depicted in Figure 3f suggests that the stripe formation on the Mn_{2nd} island involves not only the intrinsic mechanism for the Mn_{1st} island but also additional factors. This interpretation is consistent with the difference in underlying substrates; the Mn_{2nd} is formed on the Mn_{1st},

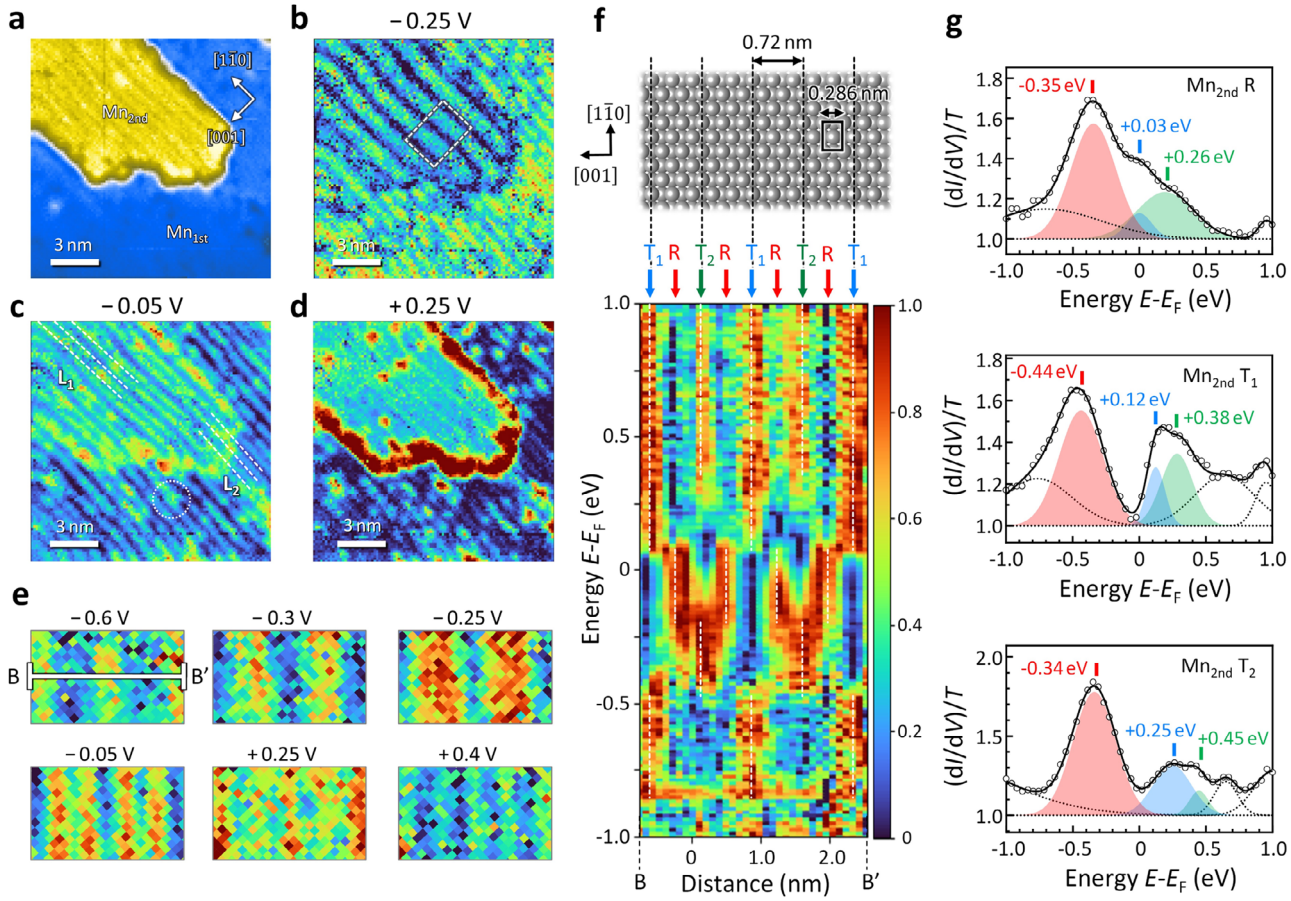

Figure 3. Electronic structure of Mn bilayer on bcc Fe(110). a) STM topography of a surface where Mn monolayer and bilayer coexist on Fe(110), imaged at a sample bias of −1.0 V. b–d) d*I*/d*V* maps obtained simultaneously with **a** at sample biases of −250 mV, −50 mV, 250 mV. Images a-d cover the same 15 × 15 nm^2 area. In c, characteristic irregularities of the stripe pattern are marked by dotted line circles and broken lines (labeled L_1 and L_2). e) d*I*/d*V* maps at various characteristic bias voltages, extracted from a boxed area in b. f) A d*I*/d*V* profile map along line B-B' in image **e**, as a function of energy relative to the Fermi level (E_F). Each profile is normalized within [0, 1]. At the top of **d**, the atomic structural model of the Fe(110) surface is shown for reference. Two distinctive trench and ridge regions in the stripe pattern at a bias of -50 mV are indicated by arrows'T1', 'T2', and 'R' respectively. g) Normalized d*I*/d*V* spectra at R, T_1, and T_2 areas. The spectral peak positions near Fermi Energy, marked by red, blue, and green ticks, were derived from Gaussian fitting analysis.

and the Mn_{1st} is formed on a Fe(110) surface. The substrate dependence likely causes variations in their electronic structures. To verify this, we analyzed normalized d*I*/d*V* spectra from three representative areas of the stripe pattern, labeled R, T_1, and T_2 in Figure 3f, as presented in Figure 3g. The spectral shapes in these three regions are distinct from those observed on the Mn_{1st} island (Figure 2g). Notably, within the Mn_{2nd} island, the spectral shapes vary significantly across regions R, T_1, and T_2, as further highlighted in the direct comparison in Figure S4d (Supporting Information). Gaussian fitting analysis of these spectra revealed distinct LDOS peak positions near the Fermi energy, marked by red, blue, and green ticks in Figure 3g. For the R site, the peaks are located at −0.35, +0.03, and +0.26 eV. In comparison, for the T_1 site, the peaks shift to −0.44, +0.12, and +0.38 eV, while for the T_2 site, they shift to −0.34, +0.25, and +0.45 eV. These variations in peak positions, ranging from 100 to 220 meV, are larger than those observed on the Mn_{1st} layer (see Figure 2g), where the shifts are limited to 20–70 meV. This pronounced difference highlights the variations in electronic structures and interatomic interactions across the different sites in the Mn_{2nd} layer, which are responsible for the diverse stripe pattern.

3. Discussion

3.1. Key Factors Underlying 1D Stripe Formation in Mn/Fe Systems

For the 1D stripe formation, the role of defects is negligible (see Note S1, Supporting Information); indicating that the observed pattern reflects an intrinsic property of the Mn/Fe(110) system. To discuss the possible origins, it is essential to consider the following key aspects. Bulk crystalline Mn possesses a highly complex unit cell containing 58 atoms, and ab-initio calculations have shown that the magnetic moments are intrinsically non-collinear.[43,44] In contrast, previous studies have revealed that Mn/Fe interfaces display distinct magnetic couplings.[45,46,35–37] In particular, ultrathin Mn films pseudomorphically grown on a bcc Fe(001), a crystallographic analogue of the present

Mn/Fe(110) interface, exhibit a layer-wise AFM stacking of Mn monolayers with in-plane FM order,[35–37] a configuration that remains stable even at 300 K.[38–40] However, 1D electronic stripe patterns have not been reported in such systems,[12,34,47,42,48–53] suggesting that additional structural or magnetic interactions may be necessary to stabilize these patterns.

Hexagonal symmetry is one candidate for enhancing magnetic frustration,[54,55] potentially giving rise to a non-collinear 120-degree magnetic order (Neél state).[56,57] While an ideal hexagonal lattice is typically found in face-centered cubic (fcc) or hexagonal close-packed (hcp) systems, a quasi-hexagonal structure can also emerge on densely-packed bcc(110) plane.[58–60] On Cu(111) substrate, the energy barrier between bcc-Fe(110) and fcc-Fe(111) phases is relatively small (≈30–60 meV), potentially leading to magneto-electric coupling.[61–63] Additionally, 2D hexagonal Mn planes are known to host a variety of exotic magnetic topological phases in bulk compounds, such as a skyrmion phase in MnSi crystal,[64] a topological phase in $MnBi_2Te_4$ layered crystal,[65] and altermagnetism in MnTe crystal.[66,67] Even on nonmagnetic substrates such as W(110), 1D atomic rows of Mn have been observed at 300 K,[68] attributed to strain-driven surface reconstruction caused by lattice mismatch. In contrast, Mn 2D films exhibit a uniform p(1 × 1) LDOS in such systems. These findings suggest that the interplay of strain, lattice symmetry, and magnetic interactions is crucial in stabilizing 1D stripe patterns within Mn-based systems.

3.2. Mechanisms Behind the Observed Stripe Pattern in Mn Monolayers

Our experimental results suggest that the stripe pattern on Mn_{1st} islands primarily originates from variations in atomic arrangement and the associated modulation of the LDOS (Figure 2g). In contrast, the stripe pattern on the Mn_{2nd} island involves additional complexity due to site-dependent local electronic states (Figure 3g). Therefore, we focus our discussion here on the Mn_{1st} island to address the fundamental origin of stripe formation.

Given that Mn and Fe have nearly identical atomic radii (Mn: 0.127 nm, Fe: 0.126 nm), Mn is expected to grow pseudomorphically on the Fe substrate. Indeed, Mn film on Fe(001) adopts a p(1 × 1) structure up to a few MLs, while transforming into a bct structure.[42,69,70] On Fe(110), however, the surface has the highest atomic density among the low-index planes of bcc crystals and exhibits quasi-hexagonal symmetry, likely enhancing additional geometrical frustration that may contribute to the stripe formation.

To examine the possibility of pseudomorphic growth, the associated frustration, and its potential role in stripe formation in the present Mn/Fe(110) system, we performed density functional theory (DFT) calculations of the local atomic and electronic structures. In our calculations, we started with the simplest cases by examining a single Mn monomer (**Figure** 4a) as well as dimer (Figure 4b,c) and trimer (Figure 4d) forms on the Fe(110) substrate. Detailed parameters of each optimized atomic structure in Figure 4a–d are summarized in Table S1 (Supporting Information). From the calculated adsorption energies, the relative stability of the Mn film in various atomic configurations can be deduced. Our calculations indicate that Mn atom preferentially absorb at the fourfold hollow (4H) site in all three forms. The occupation of 4H sites, which reflect the substrate lattice periodicity, indicates that the overlayer maintains registry with the Fe lattice, as expected for pseudomorphic growth. However, the adsorption sites of Mn dimer and trimer deviate slightly from the ideal 4H positions. For example, in the Mn dimer case, where two Mn atoms occupy nearest-neighbor (n.n.) sites (Figure 4b), the interatomic distance is 0.289 nm, ≈18% longer than that between Fe atoms (0.245 nm). Notably, the system reaches lower energy when the Mn atoms are placed at next n.n. sites with a distance of 0.301 nm (Figure 4c). These results suggest that a pseudomorphic Mn monolayer on Fe(110) is under compressive stress due to Mn—Mn interactions.

In both dimers (Figure 4b,c), the Mn spins couple ferromagnetically with each other and antiferromagnetically with the Fe(110) substrate. In contrast, in the trimer (Figure 4d), one Mn atom (labeled 3) couples ferromagnetically with the Fe substrate and antiferromagnetically with adjacent Mn atoms (labeled 1 and 2). Notably, the trimer exhibits variations in out-of-plane displacements, with the FM-coupled Mn atom (labeled 3 in Figure 4d) displaced upward by 17 pm relative to the other two. These findings indicate that, on the Mn/Fe(110) system, Mn atoms experience localized magnetic frustration arising from competing Mn—Mn and Fe—Mn interactions.

Based on Figure 4a–d, the stable adsorption site of Mn atoms in the Mn_{1st} layer are expected to be near the 4H site, suggesting pseudomorphic growth. Building on this insight, we extended our calculations to the monolayer to explore stable atomic configurations. Figure 4e–h presents the optimized structures with systematically varied in-plane spin alignments. Detailed structural parameters are summarized in Table S1 (Supporting Information). Our calculations revealed that an in-plane FM Mn monolayer (Figure 4e,f) exhibits negligible energy difference between FM and AFM coupling with the Fe substrate, and no surface corrugation was found in either case. In contrast, in-plane AFM configuration (Figure 4g) is ≈300 meV per atom more stable than the in-plane FM configurations. Notably, in this model, Mn atoms with FM coupling to the substrate are displaced upward by 23 pm relative to those with AFM coupling, indicating frustration-induced corrugation even in the Mn monolayer.

Figure 4g demonstrates that atomic corrugation is induced by local magnetic frustration, which is expected to slightly modulate the local electronic structures. However, the simulated STM image for the in-plane AFM configuration (Figure S5, Supporting Information) fails to reproduce the stripe periodicity observed in our experiments: the model in Figure 4g predicts a periodicity of 0.286 nm along the [001] direction while the STM measurements (Figure 2) reveal a periodicity of 0.72 nm. This discrepancy suggests that a more complex spin alignment may underlie the observed pattern. To explore this possibility, we examined an alternative stable configuration in Figure 4h, where Mn spins are uniformly aligned along the $[1\bar{1}0]$ direction and coupled across [001] in a sequence of AFM, AFM, FM, AFM, and AFM. In this row-wise AFM/FM model, the Mn atoms exhibit distinct out-of-plane displacements, with the height from the substrate of Mn1 reaching 220 pm, while Mn2 and Mn5 are lower at 191 pm, and Mn3 and Mn4 at intermediate levels of 211 pm, as summarized in Table S1 (Supporting Information). This vertical modulation

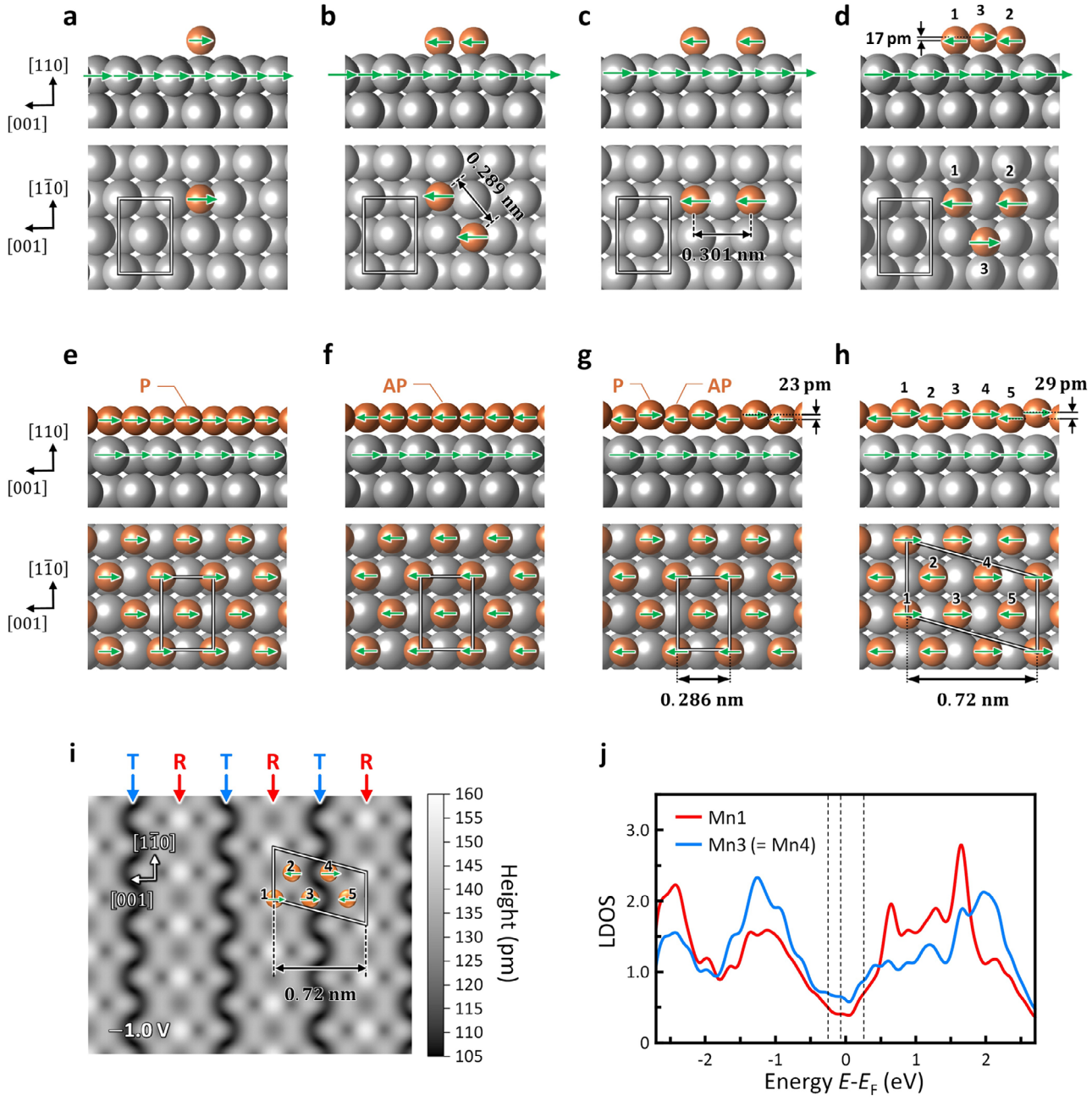

Figure 4. DFT-calculated models of various Mn configurations on the Fe(110) surface. a–h) Side (top) and top (bottom) views of Mn configurations on the Fe(110) surface: A Mn monomer located at a 4H site. A Mn dimer with each Mn atom occupying the nearest neighbor 4H sites. A Mn dimer with each Mn atom occupying the next-nearest neighbor 4H-site. A Mn trimer with one Mn pair located at the nearest neighbor 4H site and two Mn pairs located at the next-nearest neighbor 4H sites. Mn monolayer exhibiting FM coupling with the Fe(110) substrate. A Mn monolayer exhibiting AFM coupling with the Fe(110) substrate. A Mn monolayer exhibiting in-plane AFM ordering. Mn monolayer exhibiting in-plane row-wise FM/AFM ordering. Green arrows in a-h indicate the orientation of magnetic moments. i) Simulated STM topography ($V_s = -1$ V) based on the model shown in h. The apparent height is defined as the distance from the sample surface atoms to the constant-current isosurface. Arrows labeled 'T' and 'R' indicate the trench and ridge regions of the stripe pattern, respectively (see Figure 2f). j) Calculated LDOS at Mn1 (red curve) and Mn3 (= Mn4) in h. Mn1 is in the ridge region, while Mn3 (= Mn4) is in the trench region. Thus, this comparison highlights the differences in the electronic states between the two regions.

arises from the competing magnetic interaction, FM or AFM, with both the underlying Fe substrate and neighboring Mn atoms within the same monolayer. Such interdependent structural and magnetic relaxation indicates that no single spin configuration can simultaneously satisfy all exchange interactions, highlighting the emergence of magnetic frustration. While Mn atoms remain adsorbed near the 4H sites, consistent with pseudomorphic growth on Fe(110), the resulting superstructure reflects this frustrated state and is described by matrix notation $\begin{pmatrix} 3 & 2 \\ -1 & 1 \end{pmatrix}$, where

the overlayer unit vectors being linear combination of substrate lattice.

Figure 4i shows the simulated STM image of the row-wise AFM/FM model, where apparent height variations reflect the spin orientation of Mn atoms and their interactions with neighboring spins. This simulation successfully reproduces the experimentally observed stripe periodicity of 0.72 nm (λ) shown in Figure 2. We also examined the effect of the apparent height on the simulated images (see Figure S6, Supporting Information), revealing that increased apparent height reduces atomic resolution and leads to better agreement with the experimental STM images. Although the absolute tip–sample distance is not directly measurable, it is typically within sub-nm range under conventional imaging conditions (see Note S2, Supporting Information), larger than the simulated apparent height. Therefore, simulations at larger apparent height more closely reproduce the experimental images, further validating the proposed model for stripe formation.

Figure 4i also shows that the simulated range in apparent height, corresponding to the corrugation in the STM topography, is ≈55 pm (ranging from 105 to 160 pm), which is nearly twice the atomic corrugation of the row-wise AFM/FM model (29 pm). This discrepancy indicate that the observed stripe contrast cannot be explained solely by atomic corrugation but also involves subtle modulation of the LDOS between the ridge (R) and trench (T) regions, as supported by the experimental data in (Figure 2g).

Figure 4j shows the calculated LDOS for Mn1 (red curve) and Mn3 (blue curve, equivalent to Mn4), corresponding to the ridge (R) and trench (T) regions in the row-wise AFM/FM model (Figure 4h). Several spectral features appear as shoulders or bumps in the calculated LDOS, as indicated by the dashed lines, and align qualitatively with peaks observed in the experimental STS spectra (Figure 2g). Notably, the LDOS intensity differs between Mn sites, supporting the view that the observed 1D stripe contrast arises from site-dependent LDOS modulations. These results further substantiate the row-wise AFM/FM model as a plausible explanation for the experimentally observed stripe pattern.

On the other hand, our calculations show that the row-wise AFM-FM model has a slightly higher adsorption energy (by 45 meV per atom) than the in-plane AFM model (see Table S1, Supporting Information), indicating that it represents a metastable state. The structure of a film is generally influenced not only by the substrate material and its crystallographic orientation, but also by external factors such as deposition rate, substrate temperature, surface flatness, ambient environment, and the kinetic energy of the deposited species. Previous studies on organic[71] and inorganic[72] thin films have shown that nucleation at terrace sites can promote the formation of metastable structures. This tendency is attributed to the relatively low diffusion barriers on terraces, which facilitate lateral migration of adsorbed species and allow them to adopt locally stable configurations rather than global minima typically realized at step edges. Consistent with these observations, our experimental results suggest that Mn film growth on Fe(110) proceeds primarily via terrace nucleation (Figure 1c,d), making the formation of metastable structures a reasonable outcome.

Our DFT calculations (Figure 4) indicate that spin rearrangement and out-of-plane displacement of Mn atoms can relieve frustration arising from Mn—Mn and Mn—Fe interactions, thereby sustaining pseudomorphic growth of the Mn film. Alternatively, such frustration may also be relieved through lattice expansion, where Mn atoms undergo substantial in-plane displacements, leading to non-pseudomorphic growth. To examine this possibility, we investigated the structure of an Mn island on Fe(110) with 0.8 monolayer coverage (Figure S7, Supporting Information). The optimized structure relaxes into a non-pseudomorphic superstructure, where Mn atoms occupy not only the 4H site but also threefold hollow and bridge sites. A defining feature of this structure is its periodicity along the <001> direction (0.72 nm), consistent with that of the observed stripe pattern. However, the adsorption energy of this configuration (−3.59 eV atom^{-1}) is significantly higher than that of denser monolayers (see Table S1, Supporting Information), making this non-pseudomorphic superstructure is energetically unfavorable. These results further support the scenario in which the observed stripe pattern arises from spin rearrangement and out-of-plane displacements of Mn atoms under pseudomorphic growth.

3.3. Mechanisms Behind the Observed Stripe Pattern in Mn Bilayers

Finally, we discuss the mechanisms underlying the stripe formation on the Mn_{2nd} island. Our observations (Figure 3f) show that the stripes on the Mn_{2nd} island elongate along the same [1$\bar{1}$0] direction as those on the Mn_{1st} island, but with twice the periodicity. Notably, the stripe pattern exhibits a clear dependence on the applied bias voltage. While confinement of a 2D electron gas could account for the bias-dependent contrast,[73] this mechanism appears unlikely in the present case (see Note S3, Supporting Information). An alternative interpretation is that the stripe contrast arises from atomic registry between the Mn_{1st} and Mn_{2nd} islands, as suggested by the alignment of stripe elongation observed in Figure 3. This registry, along with the associated spin alignment, likely governs the stripe formation.

Considering that Mn grows pseudomorphically over several layers on Fe(001),[42] and that the Mn_{1st} layer on Fe(110) also follows the substrate lattice (as shown above), it is reasonable to infer that the Mn_{2nd} layer continues this registry, with Mn atoms occupying near the hollow sites of the Mn_{1st} layer (i.e., atop Fe atoms). However, unlike the Fe substrate, the Mn_{1st} island, which serves as the adsorption surface for the Mn_{2nd} island, exhibits a corrugated, quasi-hexagonal structure with a row-wise spin sequence of AFM, AFM, FM, AFM, and AFM. As a result, Mn atoms in the Mn_{2nd} island interact not only with the Fe substrate beneath but also with the structurally and magnetically modulated Mn_{1st} layer, experiencing a more complex local environment. This complexity may cause out-of-plane and in-plane displacements in the Mn_{2nd} layer, which break the translational symmetry of the Mn_{1st} island and give rise to site-dependent electronic states with modulated LDOS.

Based on the above discussion, we investigated the possible configurations of the Mn bilayer using DFT calculations. As the initial condition, each Mn atom in the Mn_{2nd} was placed at a hollow site of the Mn_{1st} island, while varying the Mn spin alignment under the constraint of collinearity. Due to the complex magnetic nature of Mn, DFT calculations yield multiple local minima,

making it difficult to identify the global minimum. Here, we compared a limited number of spin configurations within the experimentally observed surface unit cell. The results are presented in **Figure 5** (see Table S2, Supporting Information for optimized parameters). Additional configurations not shown in Figure 5 were also examined. In particular, initial spin alignments differing between the Mn_{1st} and Mn_{2nd} layers were explored. However, in all cases, the system converged to a solution in which the two layers share identical spin arrangements as shown in Figure 5. These calculations clearly show that corrugations in the Mn_{1st} layer is suppressed in all configurations, whereas the Mn_{2nd} layer exhibits spin-dependent out-of-plane corrugation and in-plane distortion.

Figure 5a shows the most stable structure identified, where Mn spins in both the Mn_{1st} and Mn_{2nd} layers exhibit in-plane AFM ordering. Although its periodicity (0.286 nm along [001] direction) does not match the experimentally observed value (1.44 nm), this result is reasonable given that the same spin configuration is also the most stable for the Mn_{1st} island (Figure 4g). In Figure 5b presents a row-wise AFM-FM ordering analogous to that of the Mn monolayer (Figure 4h). This structure corresponds to a metastable state, with the adsorption energy 22 meV atom^{-1} higher than that of the in-plane AFM ordering (Figure 5a), while its periodicity (0.72 nm) still deviates from the observed 1.44 nm. The calculation also revealed a similar row-wise AFM-FM configuration (Figure 5c), differing from Figure 5b only in the position of one FM-coupled Mn pair, which is shifted by two atomic sites along the [001] direction (see boxed areas in Figure 5b,c). The energy difference between the two is less than 1 meV atom^{-1}, within the computational error, indicating that they are energetically equivalent. Notably, the configuration in Figure 5c breaks the translational symmetry of the Mn_{1st} island and result in a (10 × 1) superstructure. Another (10 × 1) superstructure was found (Figure 5d), which is slightly more stable than the Figure 5c configuration by ≈6 meV atom^{-1}, making it the lowest-energy metastable state among those identified.

While the two (10 × 1) superstructures in Figure 5c,d are plausible candidates for the experimentally observed structure, unambiguously determining the actual Mn configuration remains challenging due to the presence of numerous metastable states. Nonetheless, our calculations indicate that magnetic frustration can induce both out-of-plane and in-plane lattice distortions, leading to the formation of metastable (10 × 1) superstructure. These results provide a reasonable explanation for the experimental observations.

4. Conclusion

We have demonstrated the emergence of 1D electronic stripes in ultrathin Mn films grown on a flat, non-reconstructed bcc-Fe(110) substrate. STM/STS measurements reveal that the Mn monolayer exhibits periodic rows along the [1$\bar{1}$0] direction with a 0.72 nm period, originating from LDOS modulation. These 1D stripes persist even in the second Mn monolayer, with enhanced phase variations and a doubled periodicity of 1.44 nm. DFT calculations indicate that the stripes formation arise from magnetic frustration between FM and AFM interactions, promoted by the quasi-hexagonal symmetry of the bcc(110) surface. The robustness of this pattern, stable at 300 K and insensitive to defects, suggests its utility as a 1D nanopatterning templates. Such structure based on FM/AFM interfaces could enable dimensionally controlled nanodevices, including spintronics and molecular electronics. Future studies with spin-polarized STM and exchange bias measurements, along with advanced first-principles calculations, may elucidate the role of magnetism in stabilizing these textures.

5. Experimental Section

UHV-STM Setup: All experiments were performed using a home-built UHV-STM setup (base pressure < 8.0 × 10^{-9} Pa) at 300 and 78 K,[74,75] consisting of an introduction, a preparation, and an STM analytical chamber. These separate chambers were interconnected by gate valves through which samples and STM tips were transferred in situ by using transfer rods. A UHV cryostat (CryoVAC) in the analytical chamber was used to cool down the STM stage.

Sample Preparations: A bcc-Fe(110) whisker substrate prepared by the chemical vapor deposition method[76] was introduced into the preparation chamber. The sample was subjected to repetitive cycles of Ar^+ ion sputtering (+1.0 kV, 15 min) with the substrate temperature of 873 K and post-annealing at 873 K (5 min), by which an atomically clean and flat bcc(110) surface was obtained. Mn shot (purity 99.999%, Nilaco) inserted into a Mo crucible in the preparation chamber was heated to evaporate on the Fe(110) substrate held at 300 K. The deposition rate was set at 0.25 mL min^{-1}.

STM Characterization: STM measurements were performed at 300 and 78 K. Electrochemically etched and flame-etched W-tips (φ = 0.3 mm, purity 99.99%, Nilaco),[77,78] carefully cleaned via flashing[79] in the introduction chamber prior to use, and then set into the STM stage. STM topographic images of the sample surfaces were acquired in a constant current mode. Since the apparent height in the STM topographic image includes geometric surface morphology and the electronic structure difference between the layers, it could change the evident height by ≈±20 pm. Such electronic effect in the STM images could be minimized by taking the STM image with a sample bias voltage smaller than −1 V since the tunneling at the negative bias follows the tip LDOS, which was constant on all surfaces.[12,80] LDOS on the sample surface was measured via current imaging tunneling spectroscopy (CITS), in which topographic and current-voltage (*I*–*V*) images were simultaneously recorded from the same area. Each spectrum in the *I*–*V* image was numerically differentiated to obtain d*I*/d*V*. These STM and CITS measurements were performed on multiple independently prepared samples, and the characteristic structural and electronic features were reproducibly observed across different sessions (see Figures S8 and S9, Supporting Information).

Data obtained from STM and CITS measurements were analyzed using a combination of open-source and custom-built tools, as described below. STM images were analyzed using Gwyddion. For the analysis of the d*I*/d*V* dataset, a custom Python script was employed to generate both d*I*/d*V* profile maps and d*I*/d*V* spectra. To evaluate the stripe periodicity from the profile maps, d*I*/d*V* profiles were extracted by averaging the results over voltage regions exhibiting identical stripe periodicities. The extracted profiles were then fitted using Sma4 with a multi-Gaussian function, and the stripe periodicity and its statistical uncertainty were determined from the peak positions and full width at half maximum of the fits (see Figures S10 and S11, Supporting Information). The d*I*/d*V* spectra were normalized by tunneling probability function (*T*) using Microsoft Excel to obtain the (d*I*/d*V*)/*T* curve,[41] from which the LDOS peak positions were analyzed via multi-Gaussian fitting using Sma4.

Theoretical Calculations: DFT calculations were performed with the Perdew–Burke–Ernzerhof (PBE) exchange-correlation functional using the projector-augmented-wave method implemented in the Vienna Ab initio Simulation Package (VASP) code.[81,82] The plane-wave energy cut-off was set to 400 eV. The number of *k*-points was chosen so the *k*-points distance is below 0.15 Å^{-1}. For example, for slabs with 2 × 1 surface cell

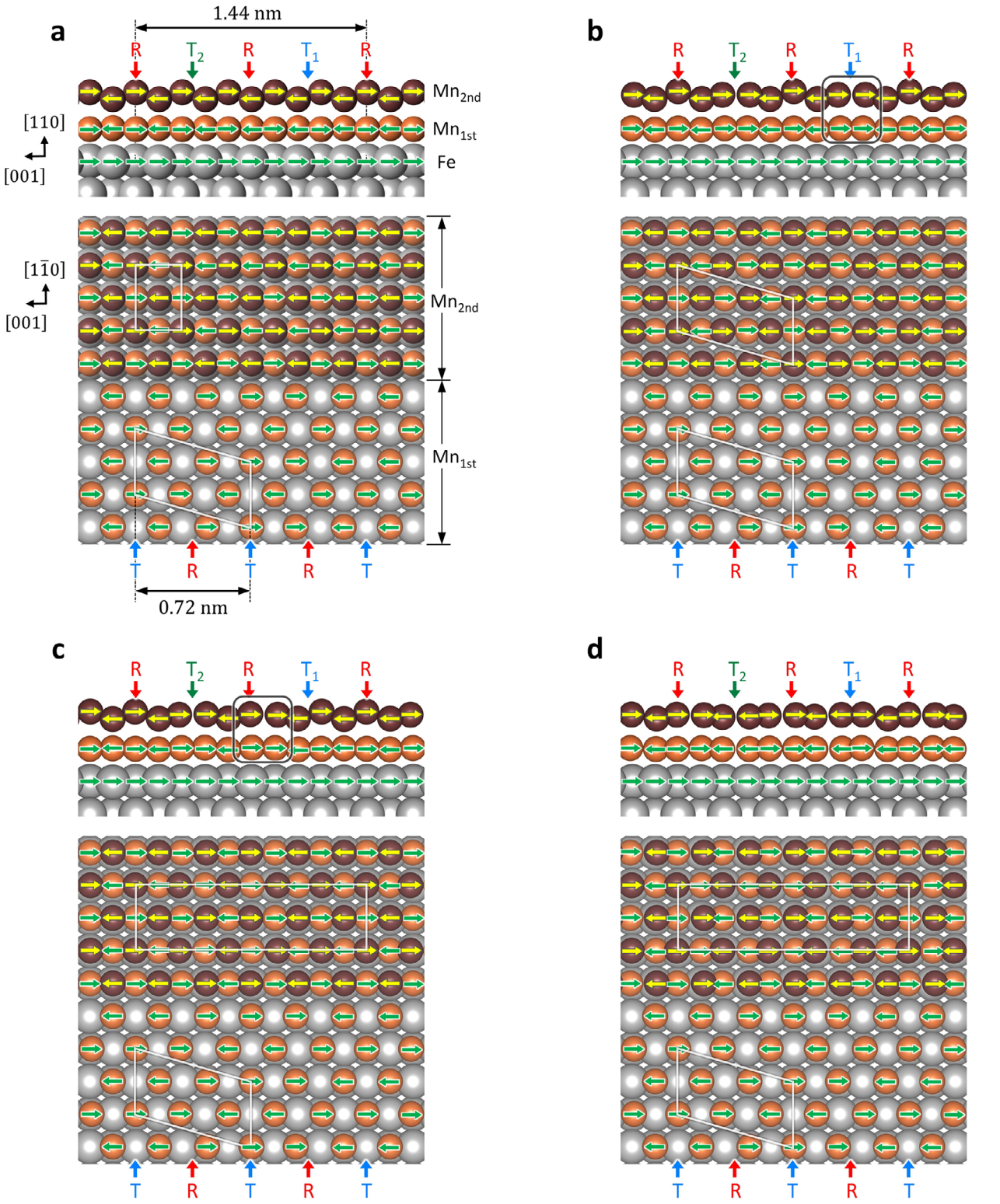

Figure 5. DFT-calculated models of Mn bilayers on Fe(110) surface. a–d) Side (top) and top (bottom) views of the Mn bilayers on the Fe(110) with various spin configurations. Arrows labeled 'T' and 'R' indicate the trench and ridge regions in the stripe pattern of the Mn_{1st} layer (see Figure 2f), while 'T_1', 'T_2', and 'R' indicate two distinct trenches and a ridge region of Mn_{2nd} layer (see Figure 3f). Green and yellow arrows represent the orientation of magnetic moments obtained from the DFT-calculations. The Mn monolayer with in-plane row-wise FM/AFM ordering is also shown as a reference in the lower part of each top view. The atoms highlighted by the boxes in **b** and **c** represent FM-coupled Mn pairs (see text for details).

(dimensions 2.8 × 4.0 Å), a 16 × 12 × 1 *k*-point mesh was used. The optimized lattice constant of bulk Fe is 2.834 Å, and the magnetic moment is 2.205 μ_B. Both values agree well with the experiment (2.86 Å, 2.22 μ_B).[83] The surface with a slab of six Fe(110) layers was modeled, of which the lower three were fixed to the bulk positions. All other atomic positions were optimized until the forces were below 0.1 eV Å^{-1}. Repeated slabs were separated by 13 Å vacuum. The results were well converged as a function of slab thickness, vacuum space, and a number of *k*-points, as it had checked with test calculations eight Fe layers, 22 Å vacuum, and *k*-point distance 0.1 Å^{-1}. Because the electron correction effect might play a role in Mn, the DFT+U approach was also tested,[84] where an effective on-site Coulomb interaction term (U–J) of 2 eV was used.[85] However, the obtained results did not differ from the DFT results (with U = J = 0) in any significant way.

Supporting Information

Supporting Information is available from the Wiley Online Library or from the author.

Acknowledgements

This work was supported by JSPS KAKENHI Grant Numbers 17K19023, 19H05789, 20H02697, 21H01812, and 23H02033. Additional support was provided by the Murata Science Foundation, the Shorai Foundation for Science and Technology, the TEPCO Memorial Foundation, the Casio Science Promotion Foundation, and the Toshiaki Ogasawara Memorial Foundation.

Conflict of Interest

The authors declare no conflict of interest.

Author Contributions

T.K.Y. conceived and designed the project. T.K.Y., E.I., and H.H. performed all STM / STS experiments. E.I. provided Python codes to analyze the STS big data, and E.I. and T.K.Y. analyzed and arranged all STM and STS data. P.K. performed DFT calculations. E.I. and T.K.Y wrote the first draft, and H.H. and P.K. corrected and added theoretical discussion in the manuscript. All authors discussed the results and commented on the manuscript.

Data Availability Statement

The data that support the findings of this study are available in the supplementary material of this article.

Keywords

antiferromagnet-ferromagnet interface, density functional theory, low-dimensional quantum structures, manganese ultrathin films, scanning tunneling microscopy

Received: April 17, 2025
Revised: August 21, 2025
Published online:

[1] T. D. Ladd, F. Jelezko, R. Laflamme, Y. Nakamura, C. Monroe, J. L. O'Brien, *Nature* **2010**, *464*, 45.
[2] N. Tombros, C. Jozsa, M. Popinciuc, H. T. Jonkman, B. J. van Wees, *Nature* **2007**, *448*, 571.
[3] S. M. Reimann, M. Manninen, *Rev. Mod. Phys.* **2002**, *74*, 1283.
[4] S. D. Sarma, S. Adam, E. H. Hwang, E. Rossi, *Rev. Mod. Phys.* **2011**, *83*, 407.
[5] P. St-Jean, V. Goblot, E. Galopin, A. Lemaître, T. Ozawa, L. L.e Gratiet, I. Sagnes, J. Bloch, A. Amo, *Nature Photon.* **2017**, *11*, 651.
[6] F. Qian, Y. Li, S. Gradečak, H. G. Park, Y. Dong, Y. Ding, Z. L. Wang, C. M. Lieber, *Nat. Mater.* **2008**, *7*, 701.
[7] J. Xiang, W. Lu, Y. Hu, Y. Wu, H. Yan, C. M. Lieber, *Nature* **2006**, *441*, 489.
[8] S. Ryu, A. P. Schnyder, A. Furusaki, A. W. W. Ludwig, *New J. Phys.* **2010**, *12*, 065010.
[9] K. Yu Arutyunov, D. S. Golubev, A. D. Zaikin, *Phys. Rep.* **2008**, *464*, 1.
[10] P. Li, F. Ding, *Sci. Adv.* **2022**, *8*, abq2900.
[11] M. M. J. Bischoff, T. K. Yamada, C. M. Fang, R. A. de Groot, H. van Kempen, *Phys. Rev. B* **2003**, *68*, 045422.
[12] T. K. Yamada, M. M. J. Bischoff, T. Mizoguchi, H. van Kempen, *Surf. Sci.* **2002**, *516*, 179.
[13] S. M. Foiles, *Surf. Sci.* **1987**, *191*, L779 .
[14] G. Binnig, H. Rohrer, C.h. Gerber, E. Weibel, *Surf. Sci.* **1983**, *131*, L379.
[15] J. Wang, M. Li, E. I. Altman, *Phys. Rev. B* **2004**, *70*, 233312.
[16] L. Floreano, A. Cossaro, R. Gotter, A. Verdini, G. Bavdek, F. Evangelista, A. Ruocco, A. Morgante, D. Cvetko, *J. Phys. Chem. C* **2008**, *112*, 10794.
[17] A. Kühnle, *Curr. Opin. Colloid Interface Sci.* **2009**, *14*, 157.
[18] D.-J. Choi, N. Lorente, J. Wiebe, K. von Bergmann, A. F. Otte, A. J. Heinrich, *Rev. Mod. Phys.* **2019**, *91*, 041001.
[19] M. F. Crommie, C. P. Lutz, D. M. Eigler, *Science* **1993**, *262*, 218.
[20] G. A. Fiete, E. J. Heller, *Rev. Mod. Phys.* **2003**, *75*, 933.
[21] B. Chen, M. Eddaoudi, S. T. Hyde, M. O'Keeffe, O. M. Yaghi, *Science* **2001**, *291*, 1021.
[22] R. S. Forgan, *Dalton Trans.* **2019**, *48*, 9037.
[23] H. Furukawa, N. Ko, Y. B. Go, N. Aratani, S. B. Choi, E. Choi, A. Ö. Yazaydin, R. Q. Snurr, M. O'Keeffe, J. Kim, O. M. Yaghi, *Science* **2010**, *329*, 424.
[24] R. Makiura, S. Motoyama, Y. Umemura, H. Yamanaka, O. Sakata, H. Kitagawa, *Nature Mater.* **2010**, *9*, 565.
[25] R. Gutzler, H. Walch, G. Eder, S. Kloft, W. M. Heckl, M. Lackinger, *Chem. Commun.* **2009**, 4456.
[26] D. Cui, D. F. Perepichka, J. M. MacLeod, F. Rosei, *Chem. Soc. Rev.* **2020**, *49*, 2020.
[27] T. K. Yamada, S. Kanazawa, K. Fukutani, S. Kera, *J. Phys. Chem. C* **2024**, *128*, 1477.
[28] F. Bischoff, W. Auwärter, J. V. Barth, A. Schiffrin, M. Fuhrer, B. Weber, *Chem. Mater.* **2017**, *29*, 9907.
[29] A. Soumyanarayanan, M. M. Yee, Y. He, J. van Wezel, D. J. Rahn, K. Rossnagel, E. W. Hudson, M. R. Norman, J. E. Hoffman, *Procee. Nat. Acad. Sci.* **2013**, *110*, 1623.
[30] R. Ichikawa, Y. K. Takahashi, E. Inami, T. K. Yamada, *npj 2D Mater Appl.* **2025**, *9*, 59.
[31] C. J. Arguello, S. P. Chockalingam, E. P. Rosenthal, L. Zhao, C. Gutiérrez, J. H. Kang, W. C. Chung, R. M. Fernandes, S. Jia, A. J. Millis, R. J. Cava, A. N. Pasupathy, *Phys. Rev. B* **2014**, *89*, 235115.
[32] U. Chatterjee, J. Zhao, M. Iavarone, R. Di Capua, J. P. Castellan, G. Karapetrov, C. D. Malliakas, M. G. Kanatzidis, H. Claus, J. P. C. Ruff, F. Weber, J. van Wezel, J. C. Campuzano, R. Osborn, M. Randeria, N. Trivedi, M. R. Norman, S. Rosenkranz, *Nat. Commun.* **2015**, *6*, 6313.
[33] D. Jiang, T. Yuan, Y. Wu, X. Wei, G. Mu, Z. An, W. Li, *ACS Appl. Mater. Interfaces* **2020**, *12*, 49252.
[34] Y. Kosuge, T. K. Yamada, *Vac. Surf. Sci.* **2020**, *63*, 459.

[35] W. Wulfhekel, U. Schlickum, J. Kirschner, *Microsc. Res. Tech.* **2005**, *66*, 105.
[36] T. k. Yamada, A. l. Vázquez de Parga, M. m. j. Bischoff, T. Mizoguchi, H. van Kempen, *Microsc. Res. Tech.* **2005**, *66*, 93.
[37] T. K. Yamada, E. Martínez, A. Vega, R. Robles, D. Stoeffler, A. L. Vázquez de Parga, T. Mizoguchi, H. van Kempen, *Nanotechnology* **2007**, *18*, 235702.
[38] D. T. Pierce, J. Unguris, R. J. Celotta, M. D. Stiles, *J. Magn. Magn. Mater.* **1999**, *200*, 290.
[39] D. T. Pierce, A. D. Davies, J. A. Stroscio, D. A. Tulchinsky, J. Unguris, R. J. Celotta, *J. Magn. Magn. Mater.* **2000**, *222*, 13.
[40] J. Unguris, R. J. Celotta, D. A. Tulchinsky, D. T. Pierce, *J. Magn. Magn. Mater.* **1999**, *198*, 396.
[41] Y. Yamagishi, S. Nakashima, K. Oiso, T. K. Yamada, *Nanotechnology* **2013**, *24*, 395704.
[42] T. K. Yamada, M. M. J. Bischoff, G. M. M. Heijnen, T. Mizoguchi, H. van Kempen, *Phys. Rev. Lett.* **2003**, *90*, 056803.
[43] D. Hobbs, J. Hafner, D. Spišák, *Phys. Rev. B* **2003**, *68*, 014407.
[44] J. Hafner, D. Spišák, *Phys. Rev. B* **2005**, *72*, 144420.
[45] A.-O. Mandru, J. Pak, A. R. Smith, J. Guerrero-Sanchez, N. Takeuchi, *Phys. Rev. B* **2015**, *91*, 094433.
[46] J. Guerrero-Sánchez, A.-O. Mandru, N. Takeuchi, G. H. Cocoletzi, A. R. Smith, *Appl. Surf. Sci.* **2016**, *363*, 651.
[47] M. M. J. Bischoff, T. Yamada, A. J. Quinn, H. van Kempen, *Surf. Sci.* **2002**, *501*, 155.
[48] T. K. Yamada, M. M. J. Bischoff, G. M. M. Heijnen, T. Mizoguchi, H. V. Kempen, *Jpn. J. Appl. Phys.* **2003**, *42*, 4688.
[49] T. K. Yamada, M. M. J. Bischoff, A. L. Vázquez de Parga, T. Mizoguchi, H. van Kempen, *Surf. Sci.* **2004**, *558*, 201.
[50] T. K. Yamada, R. Robles, E. Martinez, M. M. J. Bischoff, A. Vega, A. L. V. de Parga, T. Mizoguchi, H. van Kempen, *Phys. Rev. B* **2005**, *72*, 014410.
[51] T. K. Yamada, A. L. Vázquez de Parga, M. M. J. Bischoff, T. Mizoguchi, H. van Kempen, *Surf. Sci.* **2006**, *600*, 1048.
[52] A. Bagrets, S. Schmaus, A. Jaafar, D. Kramczynski, T. K. Yamada, M. Alouani, W. Wulfhekel, F. Evers, *Nano Lett.* **2012**, *12*, 5131.
[53] T. K. Yamada, A. L. Vazquez de Parga, *Appl. Phys. Lett.* **2014**, *105*, 183109.
[54] J.-J. Jiang, F. Tang, C.-H. Yang, *J. Phys. Soc. Jpn.* **2015**, *84*, 124710.
[55] B. Göbel, I. Mertig, O. A. Tretiakov, *Phys. Rep.* **2021**, *895*, 1.
[56] J. A. Sears, L. E. Chern, S. Kim, P. J. Bereciartua, S. Francoual, Y. B. Kim, Y.-J. Kim, *Nat. Phys.* **2020**, *16*, 837.
[57] L. Holleis, J. C. Prestigiacomo, Z. Fan, S. Nishimoto, M. Osofsky, G.-W. Chern, J. van den Brink, B. S. Shivaram, *npj Quantum Mater.* **2021**, *6*, 66.
[58] A. Biedermann, W. Rupp, M. Schmid, P. Varga, *Phys. Rev. B* **2006**, *73*, 165418.
[59] L. Gerhard, M. Peter, W. Wulfhekel, *Phys. Rev. B* **2015**, *91*, 184107.
[60] P.-J. Hsu, J. Kügel, J. Kemmer, F. Parisen Toldin, T. Mauerer, M. Vogt, F. Assaad, M. Bode, *Nat Commun.* **2016**, *7*, 10949.
[61] T. K. Yamada, L. Gerhard, T. Balashov, A. F. Takács, R. J. H. Wesselink, W. Wulfhekel, *Jpn. J. Appl. Phys.* **2011**, *50*, 08LA03.
[62] L. Gerhard, T. K. Yamada, T. Balashov, A. F. Takacs, R. J. H. Wesselink, M. Dane, M. Fechner, S. Ostanin, A. Ernst, I. Mertig, W. Wulfhekel, *IEEE Trans. Magn.* **2011**, *47*, 1619.
[63] L. Gerhard, T. K. Yamada, T. Balashov, A. F. Takács, R. J. H. Wesselink, M. Däne, M. Fechner, S. Ostanin, A. Ernst, I. Mertig, W. Wulfhekel, *Nature Nanotech.* **2010**, *5*, 792.
[64] T. Nakajima, H. Oike, A. Kikkawa, E. P. Gilbert, N. Booth, K. Kakurai, Y. Taguchi, Y. Tokura, F. Kagawa, T. Arima, *Sci. Adv.* **2017**, *3*, 1602562.
[65] J.-Q. Yan, Q. Zhang, T. Heitmann, Z. Huang, K. Y. Chen, J.-G. Cheng, W. Wu, D. Vaknin, B. C. Sales, R. J. McQueeney, *Phys. Rev. Mater.* **2019**, *3*, 064202.
[66] J. Krempaský, L. Šmejkal, S. W. D'Souza, M. Hajlaoui, G. Springholz, K. Uhlířová, F. Alarab, P. C. Constantinou, V. Strocov, D. Usanov, W. R. Pudelko, R. González-Hernández, A. Birk Hellenes, Z. Jansa, H. Reichlová, Z. Šobáň, R. D. Gonzalez Betancourt, P. Wadley, J. Sinova, D. Kriegner, J. Minár, J. H. Dil, T. Jungwirth, *Nature* **2024**, *626*, 517.
[67] L. Šmejkal, J. Sinova, T. Jungwirth, *Phys. Rev. X* **2022**, *12*, 040501.
[68] M. Bode, S. Heinze, A. Kubetzka, O. Pietzsch, M. Hennefarth, M. Getzlaff, R. Wiesendanger, X. Nie, G. Bihlmayer, S. Blügel, *Phys. Rev. B* **2002**, *66*, 014425.
[69] S. K. Kim, Y. Tian, M. Montesano, F. Jona, P. M. Marcus, *Phys. Rev. B* **1996**, *54*, 5081.
[70] S. Andrieu, H. Fischer, E. Foy, P. Lefevre, M. Alnot, M. Piecuch, *J. Magn. Magn. Mater.* **1999**, *198*, 285.
[71] G. Hlawacek, P. Puschnig, P. Frank, A. Winkler, C. Ambrosch-Draxl, C. Teichert, *Science* **2008**, *321*, 108.
[72] R. Shimizu, K. Yamamoto, T. Suzuki, T. Ohsawa, S. Shiraki, T. Hitosugi, *Thin Solid Films* **2015**, *595*, 153.
[73] L. Bürgi, O. Jeandupeux, A. Hirstein, H. Brune, K. Kern, *Phys. Rev. Lett.* **1998**, *81*, 5370.
[74] T. K. Yamada, R. Nemoto, F. Nishino, T. Hosokai, C.-H. Wang, M. Horie, Y. Hasegawa, S. Kera, P. Krüger, *J. Mater. Chem. C* **2024**, *12*, 874.
[75] R. Nemoto, P. Krüger, A. N. Putri Hartini, T. Hosokai, M. Horie, S. Kera, T. K. Yamada, *J. Phys. Chem. C* **2019**, *123*, 18939.
[76] T. K. Yamada, Y. Yamagishi, S. Nakashima, Y. Kitaoka, K. Nakamura, *Phys. Rev. B* **2016**, *94*, 195437.
[77] T. Yamaguchi, E. Inami, Y. Goto, Y. Sakai, S. Sasaki, T. Ohno, T. K. Yamada, *Rev. Sci. Instrum.* **2019**, *90*, 063701.
[78] Y. Goto, R. Suizu, Y. Noguchi, T. K. Yamada, *Appl. Surf. Sci.* **2021**, *542*, 148642.
[79] T. K. Yamada, T. Abe, N. M. K. Nazriq, T. Irisawa, *Rev. Sci. Instrum.* **2016**, *87*, 033703.
[80] V. A. Ukraintsev, *Phys. Rev. B* **1996**, *53*, 11176.
[81] G. Kresse, J. Furthmüller, *Phys. Rev. B* **1996**, *54*, 11169.
[82] G. Kresse, D. Joubert, *Phys. Rev. B* **1999**, *59*, 1758.
[83] C. Kittel, P. McEuen, *Introduction to Solid State Physics*, John Wiley & Sons, Hoboken, New Jersey, USA **2018**.
[84] J. P. Corbett, J. Guerrero-Sanchez, A. L. Richard, D. C. Ingram, N. Takeuchi, A. R. Smith, *Appl. Surface Sci.* **2017**, *422*, 985.
[85] I. Di Marco, J. Minár, S. Chadov, M. I. Katsnelson, H. Ebert, A. I. Lichtenstein, *Phys. Rev. B* **2009**, *79*, 115111.